International Journal of Thermal Sciences 207 (2025) 109392

Contents lists available at ScienceDirect

International Journal of Thermal Sciences

journal homepage: www.elsevier.com/locate/ijts

High-performance long-wavelength infrared switchable stealth based on In_3SbTe_2 metasurface

Guoqing Xu [a,1], Qianlong Kang [a,1], Xizheng Zhang [b], Wei Wang [c], Kai Guo [a], Zhongyi Guo [a,*]

[a] School of Computer and Information, Hefei University of Technology, Hefei, 230009, China
[b] School of Materials Science and Engineering, Hefei University of Technology, Hefei, 230009, China
[c] Department of Mathematics and Physics, Shijiazhuang Tiedao University, Shijiazhuang, 050043, China

ARTICLE INFO

Keywords:
Metasurface
Phase change material (PCM)
Long-wavelength infrared (LWIR)
Thermal stealth
Thermal management

ABSTRACT

Metasurface based on phase change material (PCM) for switchable thermal radiation is of great significance to the application of infrared (IR) stealth and thermal management in multi-scenario. However, the previously reported results based on GST and VO_2 metasurface face the challenges of relatively low intrinsic loss in metallic state and weak stability, respectively. In this paper, we have designed a plasmonic metasurface thermal emitter (PMTE) based on the PCM of In_3SbTe_2 (IST), which can manage the thermal emissivity in the wavelength range of 5–14 μm as the IST changes from the amorphous to the crystalline state. For IST in the amorphous state, the PMTE's average emissivity in the wavelength ranges of 5–8 μm and 8–14 μm, are 0.22 and 0.44 respectively, which can be used for the long-wavelength IR (LWIR) stealth of object with low temperature in high-temperature environment. For IST in the crystalline state, the PMTE's average emissivity in the wavelength ranges of 5–8 μm and 8–14 μm, are 0.68 and 0.14 respectively, which can achieve radiative heat dissipation and LWIR stealth of object with high temperature in low-temperature environment. We displayed simulated infrared images of the PMTE in amorphous and crystalline states to demonstrate its switchable LWIR stealth at different temperatures. In addition, the radiative heat dissipation properties of the PMTE are discussed. Our proposed PMTE based on IST can be potentially applied to IR stealth and thermal management in different scenarios.

1. Introduction

Any object with temperature above absolute zero will generate infrared (IR) thermal radiation and the temperature determines the thermal radiation spectrum which could be described by the Planck's law [1]. The long-wavelength IR (LWIR) band of 8–14 μm, known as the atmospheric transparent window, is of significant interests since a large portion of thermal emission is concentrated in this band [2–4]. Therefore, the LWIR thermal imaging system has been extensively utilized to detect and recognize objects, including various military targets and equipment [5–7]. To counter it, a variety of IR stealth technologies, which can reduce the intensity difference in thermal radiation between object and background, have been widely proposed [8]. According to the Stefan-Boltzmann law, the thermal radiation intensity of an object is proportional to the surface emissivity (ε) and fourth power of its temperature (T) [9]. As a result, the IR stealth of objects with high temperature is very challenging. It is effective and convenient to regulate thermal radiation intensity of an object by controlling its emissivity [10–13]. To this end, the traditional coating technology for IR stealth has been demonstrated through its low emissivity in the working bands of IR detector [14–16]. However, it suffers from lacking of thermal stability and switching ability in multi-scenario. There is an urgent requirement for switchable LWIR stealth and thermal management at present.

Over the past decades, a tremendous amount of effort has been attributed to the switchable IR thermal radiation for the switchable IR stealth and thermal management. Researchers have begun to develop advanced materials and applying them to nanophotonic structures to realize their full potential as switchable thermal emitters. According to different external excitations, these switchable emitters can be categorized into four types. (i) Thermally responsive emitters, which achieve switchable thermal emission by changing the material properties through heating. The most commonly used materials in this category are phase change materials (e.g., GST, VO_2, etc.) [17–20]. (ii) Electrically

* Corresponding author.
E-mail address: guozhongyi@hfut.edu.cn (Z. Guo).
[1] G. Xu and Q. Kang contribute to this work equally.

https://doi.org/10.1016/j.ijthermalsci.2024.109392
Received 2 May 2024; Received in revised form 10 August 2024; Accepted 30 August 2024
Available online 2 September 2024

responsive emitters, which achieve switchable thermal emission by the redox reactions of electrochromic materials or modulating the carrier density in graphene through voltage [21–24]. (iii) Mechanically responsive emitters, which achieve switchable thermal emission by stretching and contracting the structure through the application of external force [25]. (iv) Humidity responsive emitters, which achieve switchable thermal emission by wetting or drying porous polymer structures or hydrogels [26]. Among them, the most popular concepts are the metasurfaces based on phase change materials (PCMs) (e.g., VO_2, GST) and active materials (e.g., graphene) owing to their miniaturization.

Although, the plasmonic metasurfaces based on above tunable materials can achieve switchable IR thermal radiation, there are still some shortcomings. The graphene and VO_2 are volatile materials and require a continuous energy input to maintain their states, which is high energy consumption [22]. For example, Wang et al. proposed a tunable radiative metasurface based on graphene for information encryption and anti-counterfeiting [23]. However, the continuous application of voltage is required on the graphene to maintain the stability of the metasurface state. In comparison, the GST is nonvolatile, requiring no external power sustainment. The GST material is usually used as a spacer layer in the plasmonic metasurfaces, which can achieve switchable IR thermal radiation by the changes in effective refractive index of GST induced by annealing conditions [27–29]. However, the metallic property of GST in crystalline state is much weaker than VO_2 in metallic state, leading to a limited modulation range of the management of the IR thermal radiation. For example, Kang et al. proposed a tunable infrared emitter based on GST for infrared camouflage and thermal management [28]. However, its modulation range of thermal emission is limited. Recently, the nonvolatile PCM of In_3SbTe_2 (IST) has been successfully demonstrated in engineering the thermal emission, taking advantages of its drastic difference in refractive index between amorphous and crystalline states, which is comparable to VO_2 [30]. Nevertheless, a switchable metasurface based on the IST for LWIR stealth and thermal management still remains a challenging task.

In this paper, we propose a switchable plasmonic metasurface thermal emitter (PMTE) based on the IST, which can manipulate the spectral emissivity in the wavelength range of 5–14 μm as the IST varies from amorphous to crystalline states. Specifically, when IST is in the amorphous state, the PMTE has lower and higher spectral emissivity at 5-8 μm and 8-14 μm, respectively, which is used for the LWIR stealth of low-temperature object in high-temperature environment. In contrast, after the phase change, the PMTE has higher and lower spectral emissivity at 5-8μm and 8-14μm, respectively, which can achieve radiative heat dissipation in the 5–8 μm and LWIR stealth of high-temperature object in low-temperature environment. In addition, the simulated IR images of the PMTE are obtained in the high and low-temperature environments, which can demonstrate switchable LWIR stealth at different temperatures. Our proposed PMTE based on the IST provides a valuable reference scheme for IR stealth and thermal management in the different scenarios.

2. Structural design and spectral analysis

Fig. 1 compares the optical properties of the IST with typical materials, including metal, dielectric and PCMs. The red arrow marks out the difference in refractive index of IST between its crystalline and amorphous states. It could be seen that a drastic change happens when the state of IST changes, especially compared with GST224 and GST225 [31–33]. Although VO_2 has strong metallic properties, it still has some shortcomings. For example, VO_2 is a volatile material that requires a continuous energy input to maintain its phase change [34,35], which is energy-intensive. In contrast, GST is non-volatile and does not require external power maintenance. However, the metallic properties of GST are much weaker than the IST in the crystalline state, resulting in a limited regulatory range for its infrared thermal radiation management.

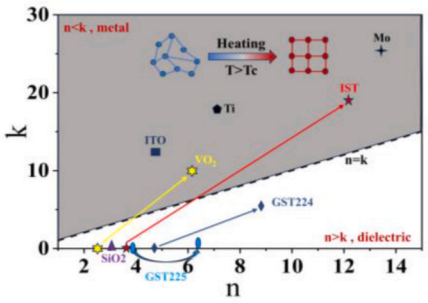

Fig. 1. Comparison of refractive indices of PCMs (IST, GST224, GST225, VO_2), metal (Mo, Ti), metal oxides (ITO), and dielectric (SiO_2) at the wavelength of 10 μm (the red, blue and yellow arrows point from amorphous to crystalline states respectively). The illustration shows schematic of the atomic structure of the IST before and after the phase change, where the temperature of phase change (T_c) is 300 °C.

Recently, the nonvolatile IST has been successfully demonstrated in the regulation of thermal emission, taking advantages of its drastic difference in refractive index between amorphous and crystalline states as shown in Fig. 1, which means greater manipulation capacity of thermal emission. That is why we choose the IST as the base PCM for our PMTE. The atomic distribution of IST in amorphous and crystalline states are shown in the illustration of Fig. 1. The atomic distribution changes from a disordered arrangement to an ordered arrangement, which is the main reason for the change of the IST's optical properties.

Fig. 2(a) shows the structure schematic of the switchable PMTE based on IST. It can be used for infrared stealth of high-temperature objects to avoid detection by infrared detectors. The PMTE can remain stable below 410 °C, making it suitable for the surface of most infrared heat sources [30,36]. When the temperature exceeds the phase change temperature of the IST (300 °C) [37], the state of IST will change from the amorphous state to crystalline state. As results, the radiation intensity of PMTE will be reduced and enhanced in the IR region of 8–14 μm and 5–8 μm, respectively, which could make us to achieve LWIR stealth and increase thermal stability simultaneously. As shown in Fig. 2 (b), the PMTE is composed of metal discs (Au), two spacer layers (ZnS and IST) and reflector layer (Ti) from top to bottom, where the period of unit cell is P, the radius and thickness of Au disc are r and t_4, the thicknesses of reflector layer and two spacer layers are t_1, t_2, t_3. The optimized geometric parameters are summarized as follows: $P = 4.5$ μm, $r = 1.7$ μm, $t_1 = 200$ nm, $t_2 = 360$ nm, $t_3 = 600$ nm, $t_4 = 100$ nm. It is worth noting that the two spacer layers could provide more degrees of freedom to control the IR thermal radiation than a single spacer layer (dielectric or PCM layer). We can demonstrate fabrication feasibility of the proposed PMTE by fabrication method in literatures [38,39]. Firstly, the 200 nm-thick Ti, 360 nm-thick IST and 600 nm-thick ZnS films can be successively deposited on silicon substrate by magnetron sputtering. Secondly, the Au disc arrays can be fabricated by using a focused ion beam system.

The emissivity is a key parameter describing the characteristics of thermal radiation from objects. According to the Kirchhoff's law of thermal radiation, the emissivity (ε) of a reciprocal system equals to the

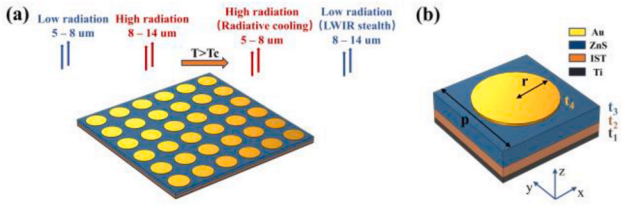

Fig. 2. (a) The schematic of the proposed PMTE based on the IST. (b) The unit cell of the proposed PMTE.

absorptivity (A) in thermal equilibrium [40,41]. For the proposed PMTE, the transmission is zero due to the presence of the reflector layer. Therefore, the spectral emissivity can be conveniently obtained from the spectral absorptivity of the PMTE by calculating A = 1-R. In this work, the proposed PMTE is numerically simulated by using a home-built program based on the finite element method [42]. In the simulation model, the port conditions and perfectly matched layers are used along the z-axis, working as open boundaries. Periodic boundary conditions are applied to boundaries in both x and y directions. The plane wave is carried out along the z-axis. In order to ensure the simulation accuracy and save time, we optimize the mesh size. Simulation details such as mesh size, boundary conditions, port conditions and simulation time adopted in the simulation are given in Table 1. The refractive indexes of Au, ZnS and Ti are obtained from Palik's book [43], and the permittivity of the IST is obtained from Ref. [44].

To demonstrate that the PMTE can achieve switchable thermal radiation in the IR region of 5–14 μm, Fig. 3(a) shows the spectral emissivity of the proposed PMTE in the amorphous and crystalline states, which are labelled as aPMTE and cPMTE, respectively. The aPMTE has low emissivity in the wavelength range of 5–8 μm and high emissivity in the wavelength range of 8–14 μm, peaking around 9.8 μm. In contrast, the spectral emissivity of cPMTE increases in the wavelength range of 5–8 μm with two emission peaks, and decreases in the wavelength range of 8–14 μm. To gain insight into the effectiveness of the proposed PMTE in achieving the switchable thermal radiation, the emissivity results with and without PMTE are compared. We use a 200 nm-thick Cr film on the silicon substrate as a reference, because Cr film is widely used for coating of objects. As shown in Fig. 3(a), compared to crystalline and amorphous PMTE, the emissivity of Cr film is lower. Although it is good for LWIR stealth in the 8–14 μm, it is not good for radiative heat dissipation in the 5–8 μm. As shown in Fig. 3(b), the spectral radiation intensity of the PMTE lies between blackbody and Cr film. It can be inferred that the Cr film/blackbody with the PMTE can achieve wavelength-selective and switchable thermal radiation in the wavelength range of 5–14 μm. Therefore, the PMTE can help objects to achieve switchable LWIR stealth and radiative heat dissipation. The radiation intensity is a physical quantity that describes the radiation ability of an object, which is helpful for analyzing the thermal radiation process and studying the radiation characteristics of an object at different temperatures. Fig. 3(b) shows the radiation intensities of the PMTE and a blackbody at the temperature of 180 °C, and the calculation process is given by the following formulas:

$$E_{PMTE}(\lambda, T) = \varepsilon_{PMTE}(\lambda) \times E_b(\lambda, T) \tag{1}$$

$$E_b(\lambda, T) = \frac{2\pi h c_0{}^2 \lambda^{-5}}{\exp[hc_0/(k\lambda T)] - 1} \tag{2}$$

where $\varepsilon_{PMTE}(\lambda)$ is the spectral emissivity, $E_b(\lambda,T)$ is the radiation intensity of the blackbody, h is the Planck's constant, c_0 is the speed of light in vacuum, k is the Boltzmann constant, λ is the wavelength and T is the temperature. It can be observed that the radiation intensity of a blackbody is larger than those of aPMTE and cPMTE, indicating that the PMTE is able to dynamically switch the IR radiation characteristics of blackbody as the IST changes from amorphous to crystalline state. In order to better illustrate the switchable characteristics of thermal emission from the PMTE, the average emissivity of PMTE in the wavelength range of 5–8 μm and 8–14 μm is calculated as follows [45]:

Table 1
Simulation parameters.

Mesh size	Port conditions	Boundary conditions	Simulation time
631 μm^3	perfectly matched layers	Periodic boundary conditions	20 min

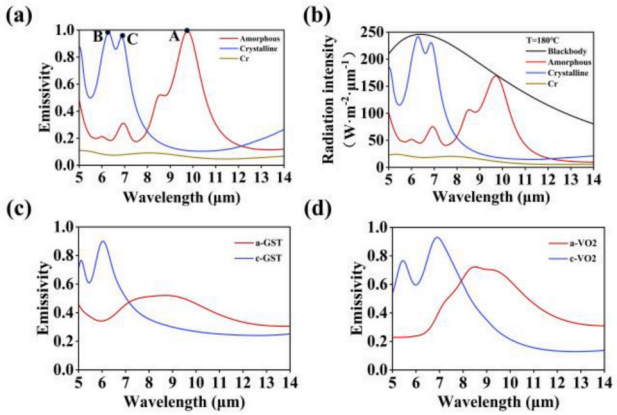

Fig. 3. (a) Simulated spectral emissivity of crystalline and amorphous PMTE and Cr film. (b) The radiation intensity of blackbody, PMTE and Cr film at 180 °C. The emissivity spectra of (c) GST-PMTE, (d) VO_2-PMTE under crystalline state and amorphous state.

$$\bar{\varepsilon}_{\lambda_1-\lambda_2} = \frac{\int_{\lambda_1}^{\lambda_2} \varepsilon_{PMTE}(\lambda) E_b(\lambda, T) d\lambda}{\int_{\lambda_1}^{\lambda_2} E_b(\lambda, T) d\lambda} \tag{3}$$

where λ_1 and λ_2 are the lower and upper limits of the wavelength, respectively. It can be calculated that the average emissivity increases from 0.22 to 0.68 and decreases from 0.44 to 0.14 in the wavelength range of 5–8 μm and 8–14 μm, respectively, when the IST changes from amorphous to crystalline state. It is known that the state change of IST is reversible [39]. The reamorphization process requires heating the IST above the melting temperature with subsequent quenching due to intrinsic cooling rates that the lattice is melt-quenched into the amorphous state. Therefore, the PMTE can achieve switchable LWIR stealth and radiative heat dissipation by controlling the phase change of IST.

To compare the advantages between IST and GST/VO_2, we numerically calculate the spectral emissivity of GST-PMTE and VO_2-PMTE in the wavelength range of 5–14 μm under crystalline state and amorphous state, which is used for quantitative comparison. As shown in Fig. 3(c) and (d), compared with GST and VO_2, the IST-PMTE has a large dynamic range of emissivity modulation in the wavelength range of 8–14 μm, which can help PMTE to achieve dynamically tunable LWIR stealth in different background environments. In addition, compared with c-GST and c-VO_2, the PMTE with c-IST has a broadband and high thermal radiation in the wavelength range of 5–8 μm and a lower emissivity in the wavelength range of 8–14 μm, which can enhance the performance of radiative heat dissipation and LWIR stealth for high temperature targets. To sum up, IST is a better candidate in our proposed metasurface structure.

3. Results and discussion

3.1. Theoretical analysis

For MIM metasurface structures, there are usually two resonance modes that affect the absorption characteristics, namely propagating surface plasmon resonance (PSPR) and local surface Plasmon resonance (LSPR) [46]. Firstly, LSPR is a local mode that exists in a very small space near the metal microstructure. When the light impinges on the metasurface, LSPRs are excited in the Au discs. The resulting charge distribution causes the inverse oscillate of electrons in the bottom metal, providing an antiparallel current distribution that produces a magnetic response. Secondly, PSPR is a special non-local mode of metal surface electrons excited by incident light, in which the metasurface can supply additional momentum to satisfy the momentum matching rule. The magnetic field of the PSPR is not only confined to the region below the

Au discs, but also in the interface between the dielectric film and the Ti film. In order to briefly demonstrate the physical mechanisms behind the three radiation peaks marked as B, C and A in Fig. 3(a), Fig. 4 presents normalized electromagnetic field distributions at these three wavelengths. It can be clearly seen that the electric fields at three points B, C and A are mainly located and enhanced at both ends of the Au discs, which is the typical feature of LSPR [47,48]. One can see that the magnetic fields at points B and C are not only confined to the ZnS film between the Au disc and the IST film, but also in the interface between the ZnS film and the IST film, which could be attributed to the hybridization between a magnetic resonance and an anti-reflection resonance. One can also see that the magnetic field at point A are mainly concentrated on the interface between the IST film and the Ti film, which could show the characteristics of PSPR [49].

Next, we analyse the effect of geometric parameters on the spectral emissivity of PMTE. Except for the parameter being discussed, other parameters are same as those mentioned above. We first study the influences of geometric parameters of the unit cell on the IR thermal radiation from aPMTE. Fig. 5(a)–(d) present the spectral emissivity of aPMTE at different parameters of P, r, t_2, t_3 and t_4. Because the radiation peak in the wavelength range of 8–14 μm originates from the SPRs, the radiation peak has a red-shift as the period of unit cell and the thickness of spacer layer increase. As shown in Fig. 5(a) and (b), when the period of unit cell increases from 3.5 μm to 5.5 μm, the radiation peak gradually becomes broad in the wavelength range of 8–14 μm. On the contrary, when the radius of disc increases from 1 μm to 2 μm, the radiation peak gradually becomes narrow in the wavelength range of 8–14 μm. As shown in Fig. 5(c) and (d), when the thicknesses of IST and ZnS layers increase from 240 nm to 480 nm and from 300 nm to 800 nm, respectively, their radiation peaks have an obvious red-shift, which can be attributed to the increase of effective permittivity. Finally, as the height of Au disc increases from 100 nm to 300 nm, the spectral emissivity of aPMTE is almost constant, as shown in Fig. 5(e).

Subsequently, we study the influences of geometric parameters of the unit cell on the IR thermal radiation from cPMTE. Fig. 5(f)–(i) present the spectral emissivity of cPMTE at different parameters of P, r, t_3 and t_4. As shown in Fig. 5(f), when the period of unit cell P increases from 3.5 μm to 5.5 μm, two discrete narrowband radiation peaks gradually form the broadband radiation in the wavelength range of 5–8 μm, and meanwhile the emissivity in the wavelength range of 8–14 μm is low and has a slight change. These characteristics are beneficial for LWIR stealth and radiative heat dissipation of 5–8 μm. Because the radiation peaks in the wavelength range of 5–8 μm can be attributed to the hybridization between the magnetic resonance and the anti-reflection resonance, the radiation peaks have an obvious red-shift as the radius of Au disc and the thickness of ZnS spacer layer increase, as shown in Fig. 5(g) and (h). Specifically, when the radius of Au disc increases from 1 μm to 2 μm, one broadband radiation peak has an obvious red-shift and gradually divides into the two discrete narrowband radiation peaks in the wavelength range of 5–8 μm, and one radiation peak in the wavelength range of 8–14 μm appears and gradually moves toward the long wavelength. As shown in Fig. 5(h), when the thickness of ZnS increases from 300 nm to 800 nm, the narrowband radiation peak has an obvious red-shift and gradually becomes the broadband radiation peak in the wavelength range of 5–8 μm, meanwhile the emissivity in the wavelength range of 8–14 μm is low and has a slight change. These characteristics are beneficial for LWIR stealth and radiative heat dissipation of 5–8 μm. Finally, there is little change in the spectral emissivity of cPMTE, as the height of Au disc increases from 100 nm to 300 nm, as shown in Fig. 5(i). It can be seen that the height of Au disc has little effect on the spectral emissivity of PMTE either before or after the phase transition.

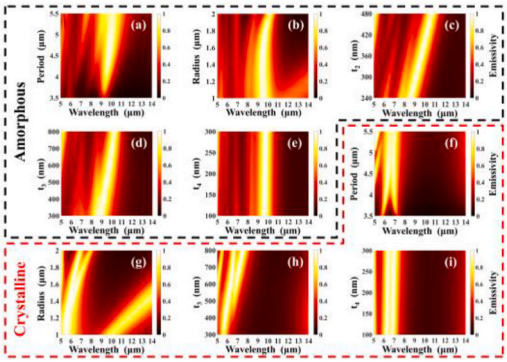

Fig. 5. The relationship between spectral emissivity of aPMTE/cPMTE and geometric parameters of unit cell. (a)–(e) The spectral emissivity of aPMTE with different periods of unit cell, radius of Au disc, thicknesses of IST layer, thicknesses of ZnS layer and heights of Au disc. (f)–(i) The spectral emissivity of cPMTE with different periods of unit cell, radius of Au disc, thicknesses of ZnS dielectric layer and heights of Au disc.

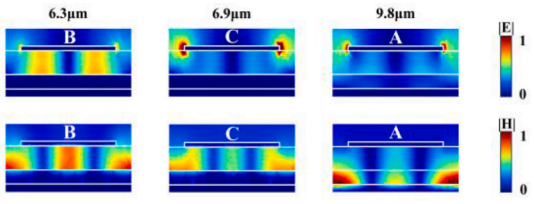

Fig. 4. The normalized electromagnetic field distribution of PMTE corresponding to three points B, C and A in Fig. 3(a).

Fig. 6 shows the spectral emissivities of aPMTE and cPMTE at different radiation angles and polarization angles. For the aPMTE, as the radiation angle increases from 0° to 70° in Fig. 6(a), the bandwidth of radiation peak in the wavelength range of 8–14 μm becomes broader and a radiation peak gradually appears in the wavelength range of 5–8 μm. These features result in the thermal radiation with broader bandwidth in the wavelength range of 5–14 μm, improving the performances of LWIR stealth of low-temperature objects in high-temperature environment. For the cPMTE, as the radiation angle increases from 0° to 70° in Fig. 6 (b), the bandwidth of radiation peak in the wavelength range of 5–8 μm becomes broader and the emissivity in the wavelength range of 8–14 μm gradually increases. This increases radiative heat dissipation of 5–8 μm, but reduces the LWIR stealth performance of high-temperature objects. Fig. 6(c) and (d) show the spectral emissivity of aPMTE and cPMTE at different polarization angles, respectively. It can be seen that the radiation spectra of aPMTE and cPMTE remain almost unchanged with the polarization angle increases from 0° to 90°, which stems from the perfect symmetry of unit cell. Therefore, the IR thermal radiation from PMTE is polarization-independent, indicating that the polarization angle does not affect the radiative heat dissipation of 5–8 μm and LWIR stealth of 8–14 μm.

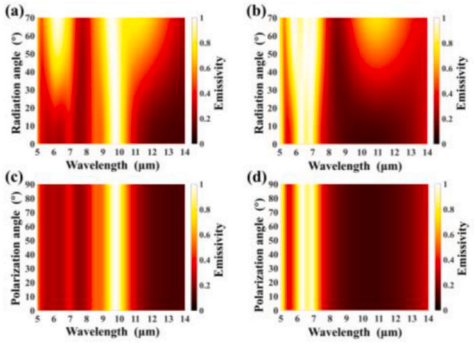

Fig. 6. The spectral emissivity of aPMTE (a) and cPMTE (b) with radiation angles varying from 0° to 70°. The spectral emissivity of aPMTE (c) and cPMTE (d) with polarization angles varying from 0° to 90°.

According to the Kirchhoff's law of thermal radiation, the radiation characteristics are consistent with absorption characteristics in a reciprocal system under the thermal-stable condition, which demonstrates that a good emitter is also a good absorber. In order to reveal the physical mechanism behind the radiation spectra of both aPMTE and cPMTE, we calculate magnetic field and power loss distributions of unit cell at different wavelengths and different positions, as shown in Fig. 7. As well know, the optical absorption could be enhanced by achieving the impedance matching, resonance mode excitation and Ohmic dissipation successively. Fig. 7(a) and (c) show the magnetic field distribution and power loss distribution of aPMTE over the 5–14 μm wavelength range, respectively. The magnetic field over the 8–14 μm wavelength range enters into the spacer layer composed by two dielectric materials and the corresponding electromagnetic wave is dissipated into the Ti reflection layer. It will lead to a radiation peak in the wavelength range of 8–14 μm. Fig. 7(b) and (d) show the magnetic field distribution and power loss distribution of cPMTE over the 5–14 μm wavelength range, respectively. Since the IST in crystalline state can be treated as a metal layer, the magnetic field over the 5–8 μm wavelength range only enters into the ZnS spacer layer and the corresponding electromagnetic wave is dissipated into the IST reflection layer. It will lead to the radiation peak in the wavelength range of 5–8 μm. On the contrary, the magnetic field over the wavelength range of 8–14 μm is weaker than those of 5–8 μm in the ZnS spacer layer and the corresponding electromagnetic wave is hardly dissipated into the IST reflection layer, which causes a little radiation in the range of 8–14 μm.

3.2. Evaluation of infrared stealth performance

As shown in Fig. 8, the LWIR thermal imager (operating band 8–14 μm) is used to obtain infrared thermal images. The PMTE sample is mounted on a vertically positioned heating plate with a background plate behind it. The LWIR thermal imager is placed in front of the sample. By adjusting the distance and focal length, the infrared thermal imager can clearly capture the sample and background plate and detect their radiation temperatures (see Fig. 9).

The three kinds of energy received by the thermal imager are shown in Fig. 8. The energy E_{sur} originates from the radiation of the surrounding environment and is then reflected from the surface of the object being measured to the thermal imager. Energy E_{obj} is blackbody spontaneous radiation and energy E_{atm} is atmospheric radiation. Therefore, in the 8–14 μm band, when the object temperature is heated to T_{obj}, the energy $E(T_{rad})$ received by the LWIR thermal imager is:

$$E(T_{rad}) = \bar{\varepsilon}\tau E(T_{obj}) + (1-A)\tau E(T_{sur}) + (1-\tau)E(T_{atm}) \quad (4)$$

where $E(T)$ is the radiant energy of 8–14 μm band of the blackbody at T, Trad is the radiation temperature, T_{obj} is the object temperature, T_{atm} is the atmosphere temperature, and T_{sur} is the surrounding environment

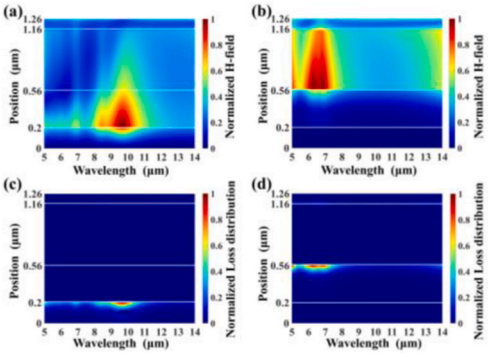

Fig. 7. Normalized H-field distributions of aPMTE (a) and cPMTE (b) over the 5–14 μm wavelength range. Normalized power loss distribution of aPMTE (c) and cPMTE (d) over the 5–14 μm wavelength range.

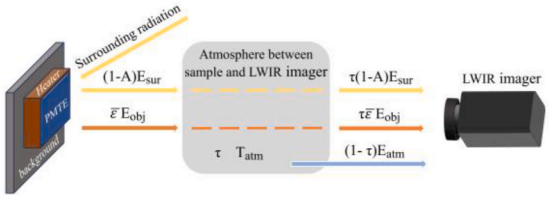

Fig. 8. Simulation schematic of radiative transfer process between object and LWIR thermal imager.

temperature. τ ($\tau \leq 1$) is the atmospheric transmittance, $\bar{\varepsilon}$ is the average emissivity of the sample in the range of 8–14 μm, and A is the average absorptivity of the sample in the range of 8–14 μm. In thermal equilibrium, $\bar{\varepsilon}$ and A are equal. The value of τ varies with the wavelength, for example, τ is close to 1 in the 8–14 μm band, and is close to 0 in the 5–8 μm band. In thermal equilibrium without atmospheric radiation, the relationship between T_{rad} and T_{obj} is given by the following formula [23]:

$$\varepsilon_0 T_{rad}^4 = \bar{\varepsilon}\tau T_{obj}^4 + (1-A)\tau T_{sur}^4 \quad (5)$$

where ε_0 is the emissivity of the IR thermal imager (usually 1) [50,51]. Since we are calculating the radiation temperature in the band 8–14 μm, the value of τ in the formula is 1 [44]. In thermal equilibrium, the average emissivity $\bar{\varepsilon} = 0$ and 1 represent perfect reflectors and blackbodies, respectively, and the average emissivity of the actual object is between 0 and 1. According to Eq. (5), when the average emissivity of the object $\bar{\varepsilon} = 0$ and 1, the radiation temperature T_{rad} is equal to the surrounding environment temperature T_{sur} and the object temperature T_{obj}, respectively.

Fig. 9 shows the relation between the radiation temperature T_{rad} and the average emissivity ($\bar{\varepsilon}$) of the object when the surrounding environment temperature (T_{sur} = 27 °C) is different from the surface temperature of the object (T_{obj} = 7–97 °C). When the surface temperature of the object is the same as the surrounding environment temperature ($T_{obj} = T_{sur}$), the radiation temperature T_{rad} does not change with the average emissivity. When the surface temperature of the object is lower than the surrounding temperature ($T_{obj} < T_{sur}$), the radiation temperature T_{rad} decreases with the increase of average emissivity. And the lower the object temperature, the faster the radiation temperature decreases with the increase of the average emissivity. When the surface temperature of the object is higher than the surrounding environment temperature ($T_{obj} > T_{sur}$), the radiation temperature T_{rad} increases with the increasing of average emissivity, and the higher the object temperature is, the faster the radiation temperature increases with the average emissivity. In the case that T_{obj} is not equal to T_{sur}, different average emissivities will correspond to different radiation temperatures. Therefore, according to the different average LWIR emissivities of the PMTE in the two states, the target can present thermal images of different colors.

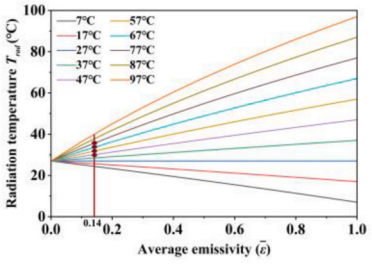

Fig. 9. The relationship between radiation temperature (T_{rad}) and average emissivity ($\bar{\varepsilon}$) at different surface temperatures (T_{obj}). The surrounding environment temperature is fixed at T_{sur} = 27 °C. The red dots represent the intersections of the average emissivity vertical ($\bar{\varepsilon}$ = 0.14) and the radiation temperature curves.

Next, we considered two application scenarios for the PMTE. In this study, the background plate is made of aluminum with an emissivity of 0.09. Firstly, we verify the LWIR stealth performance of high-temperature targets in low-temperature environments (forests, grasslands, etc.). We calculated the radiation temperature of cPMTE at T_{sur} = 27 °C, 37 °C, T_{obj} = 47 °C, 57 °C, 67 °C, 77 °C, respectively, and plotted corresponding LWIR thermal images according to the temperature field distributions, as shown in Fig. 10(a). The temperature of the background aluminum plate is maintained at 30 °C. It can be seen that the radiation temperature of cPMTE is much lower than the surface temperature, which is beneficial to the LWIR stealth of high-temperature objects. Secondly, we verified the LWIR stealth performance of low-temperature targets in high-temperature environments (deserts, workshops, etc.). We simulated LWIR thermal images of aPMTE at T_{sur} = 77 °C, 87 °C, T_{obj} = 37 °C, 47 °C, 57 °C, 67 °C, respectively, as shown in Fig. 10(b). The temperature of the background aluminum plate is maintained at 80 °C. It can be seen that the radiation temperature of aPMTE is higher than the surface temperature, which is beneficial to the LWIR stealth of low-temperature objects. The red dotted boxes indicate that the radiation temperature of the target is very close to the background temperature. It should be noted that the temperature T_{obj} and T_{sur} are not fixed and can be changed to other values according to the needs of actual application scenarios.

To comprehensively evaluate the LWIR stealth performance of the PMTE, the IR signal reduction rate $\beta(T)$ at different surface temperatures is calculated by Ref. [52]:

$$\beta(T) = \left(1 - \frac{\gamma(T)}{\delta(T)}\right) \times 100\,\% \tag{6}$$

where $\gamma(T)$ and $\delta(T)$ are the radiation intensities of the PMTE and the blackbody at temperature T, respectively. Herein, the radiation intensity of the PMTE is considered, while the environmental radiation and the solar radiation energy reflected by the emitter are ignored. $\gamma(T)$ and $\delta(T)$ are calculated using the following equations:

$$\gamma(\mathrm{T}) = \int_{\lambda_1}^{\lambda_2} \varepsilon(\lambda) E_b(\lambda, T) d\lambda \quad \delta(\mathrm{T}) = \int_{\lambda_1}^{\lambda_2} E_b(\lambda, T) d\lambda \tag{7}$$

where λ_1 and λ_2 are the lower limit and upper limit of the bandwidth, respectively. Fig. 11 shows the IR signal reduction rates of aPMTE and cPMTE as functions of temperature in the LWIR range. As the temperature increases from 300K to 700K, the signal reduction rate of the aPMTE is around 60 % and the signal reduction rate of the cPMTE is around 85 %, demonstrating that the cPMTE can better suppress the radiation intensity of blackbody than the aPMTE. The feature is useful for switchable LWIR stealth.

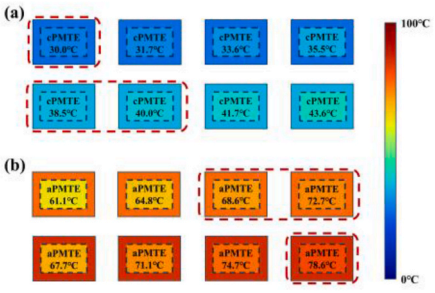

Fig. 10. (a) Simulated thermal images of cPMTE heated to 47 °C, 57 °C, 67 °C and 77 °C respectively when the background temperatures are 27 °C and 37 °C. The radiative temperatures of the background aluminum plate are 27.3 °C and 36.4 °C, respectively. (b) Simulated thermal images of aPMTE heated to 37 °C, 47 °C, 57 °C and 67 °C respectively when the background temperatures are 77 °C and 87 °C. The radiative temperatures of the background aluminum plate are 77.3 °C and 86.4 °C, respectively.

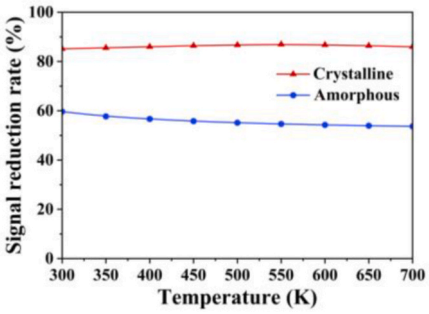

Fig. 11. The red and blue lines indicate the IR signal reduction rates of cPMTE and aPMTE in the LWIR range at different temperatures.

3.3. Evaluation of radiative heat dissipation performance

According to energy balance theory, the net radiative heat dissipation power of the PMTE is the comprehensive manifestation of the four energy flows (PMTE's radiative energy, solar energy absorption, atmospheric radiative energy and intrinsic cooling loss) [53]. Here we consider a simple scenario. On a sunny day and at room temperature, the radiative energy and solar energy absorption from the PMTE play a dominant role in the radiative heat dissipation. In order to reduce the temperature of the PMTE by radiative heat dissipation, the PMTE must have a high emissivity in the atmospheric window (8–14 μm) and high reflectivity in the solar radiation spectrum. However, the spectral requirements of radiative heat dissipation conflicts with that of LWIR stealth. To balance the spectral requirements between LWIR stealth and radiative heat dissipation, PMTE has a high emissivity in the non-atmospheric window (5–8 μm) and a low emissivity in the atmospheric window (8–14 μm).

According to the above, we can know that the radiative heat dissipation in non-atmospheric window (5–8 μm) and reflectivity in the solar radiation spectrum are important for the radiative heat dissipation of high-temperature object. Therefore, we investigate the radiated power of aPMTE and cPMTE in non-atmospheric windows. As shown in Fig. 12 (a), when the temperature increases from 300K to 650K, the radiated power of both aPMTE and cPMTE are going up. When the temperature exceeds the phase change temperature of IST, the amorphous state will not exist. Meanwhile, the radiative heat dissipation of cPMTE is much larger than that of aPMTE. The trend is consistent with the Stefan-Boltzmann law: $E = \varepsilon\sigma T^4$ (where ε is the emissivity, σ is the Stefan-Boltzmann constant, and T is the surface temperature) [54]. In addition, we simulate the reflectivity of PMTE in the solar radiation spectrum, as shown in Fig. 12(b), where the orange shaded part is the normalized spectral irradiance of solar radiation [55,56]. It can be seen that PMTE has a high reflectivity in the visible light and near-infrared spectrum, which greatly reduces the absorption of solar energy. In summary, on the basis of LWIR stealth, in order to achieve radiative heat dissipation as much as possible, PMTE need have high thermal radiation

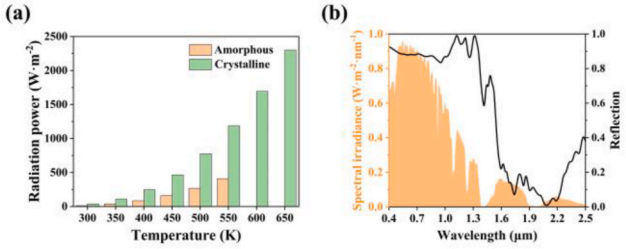

Fig. 12. (a) The radiation intensities of aPMTE and cPMTE in the wavelength range of 5–8 μm at different temperatures. (b) Spectral reflectivity of cPMTE and normalized solar spectral irradiance in the visible light and near infrared spectral ranges.

in non-atmospheric window of 5–8 μm and high reflectivity in the solar radiation spectrum.

4. Conclusions

In summary, this paper proposes a switchable plasmonic metasurface based on the IST, which realizes the functions of LWIR stealth and non-atmospheric window high radiative heat dissipation in multiple scenarios. Firstly, the method overcomes the problems of volatility and weak metal property of traditional PCMs (e.g., VO_2, GST). The structure does not require a continuous energy input to maintain the phase change and can achieve a wide range of emissivity switching. For example, the emissivity difference between the aPMTE and cPMTE are 0.89, 0.65 and 0.81 in the wavelengths of 9.8 μm, 6.9 μm and 6.3 μm, respectively. Specifically, the average emissivities of aPMTE are 0.22 and 0.44 in the wavelength ranges of 5–8 μm and 8–14 μm, which is used for the LWIR stealth of low-temperature object in high-temperature environment. The average emissivities of cPMTE are 0.68 and 0.14 in the wavelength ranges of 5–8 μm and 8–14 μm, which can achieve radiative heat dissipation in the 5–8 μm and LWIR stealth of high-temperature object in low-temperature environment. Secondly, we explain the physical mechanism of radiation peak. In addition, we evaluated the stealth performance of the PMTE and presented simulated thermal images of the PMTE at different temperatures and application scenarios. It can be seen from the simulated thermal image that the proposed PMTE has excellent LWIR stealth performance. Finally, we also evaluated the radiative heat dissipation performance of the PMTE. The work in this paper may open up new possibilities for military or civilian stealth applications, thermal management, and energy-saving devices.

CRediT authorship contribution statement

Guoqing Xu: Writing – original draft, Visualization, Validation, Software, Methodology, Investigation, Formal analysis, Data curation, Conceptualization. **Qianlong Kang:** Visualization, Supervision, Software, Methodology, Formal analysis, Conceptualization. **Xizheng Zhang:** Visualization, Methodology, Investigation, Formal analysis, Data curation. **Wei Wang:** Validation, Methodology, Investigation, Data curation. **Kai Guo:** Investigation, Formal analysis, Data curation. **Zhongyi Guo:** Writing – review & editing, Supervision, Resources, Funding acquisition, Conceptualization.

Declaration of competing interest

The authors declare that they have no known competing financial interests or personal relationships that could have appeared to influence the work reported in this paper.

Data availability

Data will be made available on request.

Acknowledgements

The authors acknowledge financial support from National Natural Science Foundation of China (NSFC) (61775050).

References

[1] W. Li, S. Fan, Nanophotonic control of thermal radiation for energy applications, Opt Express 26 (12) (2018) 15995–16021.
[2] J. Zhang, Z. Wen, Z. Zhou, D. Zhou, Q. Qiu, J. Ge, J. Hao, Long-wavelength infrared selective emitter for thermal infrared camouflage under a hot environment, Opt Express 30 (13) (2022) 24132–24144.
[3] J. Wu, B. Wu, K. Shi, X. Wu, C. Fu, Strong nonreciprocal thermal radiation of transverse electric wave in Weyl semimetal, Int. J. Therm. Sci. 187 (2023) 108172.
[4] B. Wu, X. Wu, H. Li, H. Liu, X. Huang, Spin-selective thermal radiation with near-perfect circular dichroism in twisted hyperbolic materials, Int. J. Therm. Sci. 197 (2024) 108853.
[5] M.J. Moghimi, G. Lin, H. Jiang, Broadband and ultrathin infrared stealth sheets, Adv. Eng. Mater. 20 (11) (2018) 1800038.
[6] J. Kim, C. Park, J.W. Hahn, Metal-semiconductor-metal metasurface for multiband infrared stealth technology using camouflage color pattern in visible range, Adv. Opt. Mater. 10 (6) (2022) 2101930.
[7] R. Hu, S. Zhou, Y. Li, D.Y. Lei, X. Luo, C.W. Qiu, Illusion thermotics, Adv. Mater. 30 (22) (2018) 1707237.
[8] W.F. Bahret, The beginnings of stealth technology, IEEE Trans. Aero. Electron. Syst. 29 (4) (1993) 1377–1385.
[9] H. Zhu, Q. Li, C. Tao, Y. Hong, Z. Xu, W. Shen, M. Qiu, Multispectral camouflage for infrared, visible, lasers and microwave with radiative cooling, Nat. Commun. 12 (1) (2021) 1805.
[10] Q. Kang, G. Xu, X. Zhang, W. Wang, K. Guo, Z. Guo, Broadband mid-infrared thermal emission with large degree of circular polarization enabled by symmetry-broken metasurfaces, J. Sci.: Adv. Mater. Devices (2024) 100724.
[11] Q. Kang, K. Guo, X. Zhang, W. Wang, Z. Guo, Dynamically manipulating long-wave infrared polarized thermal radiation by vanadium dioxide metasurface, Opt. Lett. 4 (2023) 101687.
[12] W. Zhang, G. Xu, J. Zhang, H. Wang, H. Hou, Infrared spectrally selective low emissivity from Ge/ZnS one-dimensional heterostructure photonic crystal, Opt. Mater. 37 (2014) 343–346.
[13] B. Wu, X. Wu, H. Liu, H. Li, X. Huang, An efficient optimization strategy applied to spacecraft smart radiation devices design, Int. J. Therm. Sci. 195 (2024) 108635.
[14] Z. Huang, W. Zhou, X. Tang, D. Zhu, F. Luo, Effects of substrate roughness on infrared-emissivity characteristics of Au films deposited on Ni alloy, Thin Solid Films 519 (10) (2011) 3100–3106.
[15] X. Yan, G. Xu, Corrosion and mechanical properties of polyurethane/Al composite coatings with low infrared emissivity, J. Alloys Compd. 491 (1–2) (2010) 649–653.
[16] Z. Huang, W. Zhou, X. Tang, Effects of annealing time on infrared emissivity of the Pt film grown on Ni alloy, Appl. Surf. Sci. 256 (7) (2010) 2025–2030.
[17] S. Chandra, D. Franklin, J. Cozart, A. Safaei, D. Chanda, Adaptive multispectral infrared camouflage, Acs Photonics 5 (11) (2018) 4513–4519.
[18] K. Tang, X. Wang, K. Dong, Y. Li, J. Li, B. Sun, J. Wu, A thermal radiation modulation platform by emissivity engineering with graded metal-insulator transition, Adv. Mater. 32 (36) (2020) 1907071.
[19] Y. Qu, Q. Li, L. Cai, M. Pan, P. Ghosh, K. Du, M. Qiu, Thermal camouflage based on the phase-changing material GST, Light Sci. Appl. 7 (1) (2018) 26.
[20] T. Wang, B. Wang, L. Li, H. Liu, K. Zhang, X. Wu, K. Yu, Coordinated multi-band stealth based on phase change materials, Int. J. Therm. Sci. 202 (2024) 109101.
[21] O. Salihoglu, H.B. Uzlu, O. Yakar, S. Aas, O. Balci, N. Kakenov, C. Kocabas, Graphene-based adaptive thermal camouflage, Nano Lett. 18 (7) (2018) 4541–4548.
[22] L. Xiao, H. Ma, J. Liu, W. Zhao, Y. Jia, Q. Zhao, K. Jiang, Fast adaptive thermal camouflage based on flexible VO_2/graphene/CNT thin films, Nano Lett. 15 (12) (2015) 8365–8370.
[23] P. Wang, J. Su, P. Ding, B. Mao, M. Ren, K. Xu, J. Wang, Graphene-metal based tunable radiative metasurface for information encryption and anticounterfeiting, Diamond Relat. Mater. 131 (2023) 109548.
[24] X. Zhang, Y. Tian, W. Li, S. Dou, L. Wang, H. Qu, Y. Li, Preparation and performances of all-solid-state variable infrared emittance devices based on amorphous and crystalline WO3 electrochromic thin films, Sol. Energy Mater. Sol. Cells 200 (15) (2019) 109916.
[25] S. Zeng, K. Shen, Y. Liu, A.P. Chooi, A.T. Smith, S. Zhai, L. Sun, Dynamic thermal radiation modulators via mechanically tunable surface emissivity, Mater. Today 45 (2021) 44–53.
[26] J. Mandal, M. Jia, A. Overvig, Y. Fu, E. Che, N. Yu, Y. Yang, Porous polymers with switchable optical transmittance for optical and thermal regulation, Joule 3 (12) (2019) 3088–3099.
[27] K.K. Du, Q. Li, Y.B. Lyu, J.C. Ding, Y. Lu, Z.Y. Cheng, M. Qiu, Control over emissivity of zero-static-power thermal emitters based on phase-changing material GST, Light Sci. Appl. 6 (1) (2017).
[28] Q. Kang, K. Guo, Z. Guo, A tunable infrared emitter based on phase-changing material GST for visible-infrared compatible camouflage with thermal management, Phys. Chem. Chem. Phys. 25 (40) (2023) 27668–27676.
[29] Q. Kang, D. Li, K. Guo, J. Gao, Z. Guo, Tunable thermal camouflage based on GST plasmonic metamaterial, Nanomater 11 (2) (2021) 260.
[30] A. Heßler, S. Wahl, T. Leuteritz, A. Antonopoulos, C. Stergianou, C.F. Schön, T. Taubner, In_3SbTe_2 as a programmable nanophotonics material platform for the infrared, Nat. Commun. 12 (1) (2021) 924.
[31] T. Cao, X. Zhang, W. Dong, L. Lu, X. Zhou, X. Zhuang, R.E. Simpson, Tuneable thermal emission using chalcogenide metasurface, Adv. Opt. Mater. 6 (16) (2018) 1800169.
[32] K. Guo, X. Li, Q. Kang, Z. Guo, Tunable full-space light field manipulation based on double-layer Ge2Sb2Te5 metasurfaces, Phys. Scripta 98 (11) (2023) 115528.
[33] K. Guo, X. Li, H. Ai, X. Ding, L. Wang, W. Wang, Z. Guo, Tunable oriented mid-infrared wave based on metasurface with phase change material of GST, Results Phys. 34 (2022) 105269.
[34] X. Fan, Q. Kang, H. Ai, K. Guo, Z. Guo, Full-space metasurface in mid-infrared based on phase change material of VO_2, J. Opt. 52 (3) (2023) 1336–1344.
[35] A. Didari-Bader, N.M. Estakhri, N. Mohammadi Estakhri, Adaptive plasmonic metasurfaces for radiative cooling and passive thermoregulation, Front Photon 4 (2023) 1193479.

[36] S.K. Pandey, A. Manivannan, Direct evidence for structural transformation and higher thermal stability of amorphous insbte phase change material, Scripta Mater. 192 (2021) 73–77.
[37] W. Zha, Y. Zhu, B. Ma, J. Yu, P. Ghosh, M. Qiu, Q. Li, Nonvolatile high-contrast whole long-wavelength infrared emissivity switching based on In_3SbTe_2, ACS Photonics 10 (7) (2022) 2165–2172.
[38] X. Jiang, H. Yuan, D. Chen, Z. Zhang, T. Du, H. Ma, J. Yang, Metasurface based on inverse design for maximizing solar spectral absorption, Adv. Opt. Mater. 9 (19) (2021) 2100575.
[39] L. Conrads, N. Honné, A. Ulm, A. Healer, R. Schmitt, M. Wuttig, T. Taubner, Reconfigurable and polarization-dependent grating absorber for large-area emissivity control based on the plasmonic phase-change material In_3SbTe_2, Adv. Opt. Mater. 11 (8) (2023) 2202696.
[40] Q. Kang, D. Li, W. Wang, K. Guo, Z. Guo, Multiband tunable thermal camouflage compatible with laser camouflage based on GST plasmonic metamaterial, J. Phys. D Appl. Phys. 55 (6) (2021) 065103.
[41] L. Wang, Y. Yang, X. Tang, B. Li, Y. Hu, Y. Zhu, H. Yang, Combined multi-band infrared camouflage and thermal management via a simple multilayer structure design, Opt. Lett. 46 (20) (2021) 5224–5227.
[42] K.J. Bathe, Finite element method. Wiley Encyclopedia of Computer Science and Engineering, 2007, pp. 1–12.
[43] E.D. Palik, Handbook of Optical Constants of Solids, vol. 3, Academic press, 1998.
[44] X. Lyu, A. Heßler, X. Wang, Y. Cao, L. Song, A. Ludwig, T. Taubner, Combining switchable phase-change materials and phase-transition materials for thermally regulated smart mid-infrared modulators, Adv. Opt. Mater. 9 (16) (2021) 2100417.
[45] R. Sun, P. Zhou, W. Ai, Y. Liu, Y. Li, R. Jiang, L. Deng, Broadband switching of mid-infrared atmospheric windows by VO_2-based thermal emitter, Opt Express 27 (8) (2019) 11537–11546.
[46] Y. Zhou, Z. Qin, Z. Liang, D. Meng, H. Xu, D.R. Smith, Y. Liu, Ultra-broadband metamaterial absorbers from long to very long infrared regime, Light Sci. Appl. 10 (1) (2021) 138.
[47] L. Yang, P. Zhou, T. Huang, G. Zhen, L. Zhang, L. Bi, L. Deng, Broadband thermal tunable infrared absorber based on the coupling between standing wave and magnetic resonance, Opt. Mater. Express 7 (8) (2017) 2767–2776.
[48] Y. Qu, Q. Li, K. Du, L. Cai, J. Lu, M. Qiu, Dynamic thermal emission control based on ultrathin plasmonic metamaterials including phase-changing material GST, Laser Photonics Rev 11 (5) (2017) 1700091.
[49] Z. Qin, D. Meng, F. Yang, X. Shi, Z. Liang, H. Xu, D.R. Smith, Y. Liu, Broadband long-wave infrared metamaterial absorber based on single-sized cut-wire resonators, Opt Express 29 (13) (2021) 20275–20285.
[50] X. Wang, Y. Lee, S. Yu, Z. Chen, J. Shiomi, S. Kim, R. Hu, Ultrahigh-efficient material informatics inverse design of thermal metamaterials for visible-infrared-compatible camouflage, Nat. Commun. 14 (1) (2023) 4694.
[51] J. Gu, H. Wei, F. Ren, H. Guan, S. Liang, C. Geng, Y. Li, VO_2-based infrared radiation regulator with excellent dynamic thermal management performance, ACS Appl. Mater. Interfaces 14 (2) (2022) 2683–2690.
[52] N. Lee, T. Kim, J.S. Lim, I. Chang, H.H. Cho, Metamaterial-selective emitter for maximizing infrared camouflage performance with energy dissipation, ACS Appl. Mater. Interfaces 11 (23) (2019) 21250–21257.
[53] B. Zhao, M. Hu, X. Ao, N. Chen, G. Pei, Radiative cooling: a review of fundamentals, materials, applications, and prospects, Appl. Energy 236 (2019) 489–513.
[54] T. Cao, M. Lian, K. Liu, X. Lou, Y. Guo, D. Guo, Wideband mid-infrared thermal emitter based on stacked nanocavity metasurfaces, Int. J. Extreme Manuf. 4 (1) (2021) 015402.
[55] K. Sun, C.A. Riedel, Y. Wang, A. Urbani, M. Simeoni, S. Mengali, O.L. Muskens, Metasurface optical solar reflectors using AZO transparent conducting oxides for radiative cooling of spacecraft, Acs. Photonics. 5 (2) (2018) 495–501.
[56] K. Sun, C.A. Riedel, A. Urbani, M. Simeoni, S. Mengali, M. Zalkovskij, O. L. Muskens, VO_2 thermochromic metamaterial-based smart optical solar reflector, Acs. Photonics 5 (6) (2018) 2280–2286.